### Nonlinear magnetic buoyancy instability and Galactic dynamo

Yasin Qazi, <sup>1</sup>\* Anvar Shukurov, <sup>1</sup> Devika Tharakkal, <sup>1,2</sup> Frederick A. Gent<sup>3,4,1</sup> & Abhiiit B. Bendre<sup>5</sup>

- <sup>1</sup>School of Mathematics, Statistics and Physics, Newcastle University, Newcastle upon Tyne, NE1 7RU, UK
- <sup>2</sup>Department of Physics, University of Helsinki, PO Box 64, FI-00014, Helsinki, Finland
- <sup>3</sup>Astroinformatics, Department of Computer Science, Aalto University, PO Box 15400, FI-00076, Espoo, Finland
- <sup>4</sup>Nordita, KTH Royal Institute of Technology and Stockholm University, Hannes Alfvéns väg 12, Stockholm, SE-106, Sweden
- <sup>5</sup>Laboratoire d'Astrophysique, EPFL, CH-1290 Sauverny, Switzerland

Accepted XXX. Received YYY; in original form ZZZ

### **ABSTRACT**

The magnetic buoyancy instability (MBI) and the Parker instability, in which cosmic rays exacerbate the MBI are strong and generic instabilities expected to occur in most astrophysical systems with sufficiently strong magnetic fields. In galactic and accretion discs, large-scale magnetic fields are thought to result from the mean-field dynamo action. in particular, the  $\alpha\omega$ -dynamo. Using non-ideal MHD equations, we model a section of the galactic disc in which the large-scale magnetic field is generated by an imposed  $\alpha$ -effect and differential rotation. We continue our earlier study of the interplay between magnetic buoyancy and the mean-field dynamo including here the differential rotation (which enhances the dynamo) and cosmic rays (which enhance magnetic buoyancy). We constructed a simple 1D model which replicated in fine detail all significant features of the 3D simulations to confirm that the inclusion of the differential rotation is responsible for the switch in field parity. The spatial pattern of the resultant magnetic field may explain the alternating magnetic field direction seen in the halo of the edge on galaxy NGC4631 or other similar galaxies such as NCG4666. With the inclusion of cosmic rays and when buoyancy is dominant, the nonlinear states are once again oscillatory.

Key words: instabilities – magnetic fields – MHD – dynamo – galaxies: magnetic fields – ISM: structure

### 1 INTRODUCTION

The magnetic buoyancy instability (MBI) Newcomb (1961), or the magnetic Rayleigh-Taylor instability is a fundamental process that affects magnetic fields in stratified plasmas. It develops wherever the strength of a (horizontal) magnetic field decreases sufficiently rapidly along the (vertical) direction opposite to the vector of gravitational acceleration. A typical situation is a flat plasma layer with a magnetic field in the layer plane and gravitational acceleration perpendicular to it, as it happens in galactic and accretion discs. Under the hydrostatic equilibrium, both magnetic field strength and gas density usually decrease with distance z from the layer midplane. Since the magnetic field has pressure but not weight, the gas density is reduced near the midplane where the magnetic field is stronger, producing an unstable structure where the weightless magnetic field, is supporting the gas. The interstellar medium of spiral galaxies also contains cosmic rays which have negligible weight but exert a dynamically significant pressure. They enhance the instability, and the MBI is modified by cosmic rays is known as the Parker instability Parker (1979). The instability is ubiquitous, its time scale (of the order of the sound or Alfvén crossing time based on the density scale height) is much shorter than the lifetimes of astrophysical objects, and it must be in its nonlinear state in virtually any object prone to it. The linear stage of the Parker instability is well understood and its dispersion relation has been obtained for a variety of physical models (e.g., Giz & Shu 1993; Foglizzo & Tagger 1994, 1995; Kim et al. 1997; Rodrigues et al. 2016, see also Shukurov & Subramanian 2021 and references therein). However, the nonlinear, quasi-stationary states of the MBI and Parker instability are much less understood, in particular, because they require numerical simulations. Tharakkal et al. (2023b,a) investigated the non-linear states of the MBI and Parker instability of an imposed horizontal, unidirectional magnetic field. In a non-rotating system, the instability leads to a state with very large scale heights of both magnetic field and cosmic rays, the subsequent gas layer is thin as it is supported solely by the thermal pressure gradient (and turbulent pressure if available) (Tharakkal et al. 2023b). Rotation changes the nonlinear state significantly because gas motions driven by the instability become helical and can act as a mean-field dynamo (e.g., Tharakkal et al. 2023a, see also Hanasz & Lesch 1997 and Moss et al. 1999 and references therein). As a result, the magnetic field near the midplane changes profoundly and can even reverse its direction in what appears to be a nonlinear. long-period oscillation. Similar magnetic field reversals occur in the simulations of Johansen & Levin (2008), Gaburov et al. (2012) and Machida et al. (2013). Large-scale magnetic fields in galaxies and accretion discs are produced by a mean-field ( $\alpha$ -effect) dynamo (Shukurov & Subramanian 2021, and references therin), and Qazi et al. (2023) explore the nonlinear instability of a magnetic field generated by the imposed  $\alpha$ -effect rather than imposed directly via initial or boundary conditions. Rotation is neglected in this model to simplify the interaction of the dynamo and

<sup>\*</sup> E-mail: Y.Qazi@newcastle.ac.uk

the MBI. Magnetic fields generated by the  $\alpha$ -effect are helical, and the Lorentz force drives helical motions which act as a dynamo. As a result, the system develops nonlinear oscillations similar in their origin to those observed by Tharakkal et al. (2023a) in a rotating system.

Here we extend the model of Qazi et al. (2023) to explore the effects of rotation and cosmic rays on the MBI. We confirm that the nonlinear state can be oscillatory and the large-scale magnetic field can change its parity from a quadrupolar oscillatory field (where the horizontal magnetic field is symmetric with respect to the midplane) to a dipolar non-oscillatory state (where the horizontal field is antisymmetric).

The problem is formulated in Section 2. The effects of the Coriolis force and differential rotation, additionally, as the helicity of the gas flows driven by the instability which emerges because of the Coriolis and Lorentz forces are discussed in Section 3. In Section 6 we develop the one-dimensional model described in Section 4.1 of Qazi et al. (2023) for the instability and the associated dynamo to replicate the effects of the simulations in Section 3. Cosmic rays are included in Section 7 where we also consider viscosity and magnetic diffusivity values similar to those produced by the supernova-driven turbulence in spiral galaxies. Section 8 summarizes our results in a brief form.

The question we wish to address is how the rotation will alter the nonlinear states of the magnetic buoyancy instability. We present simulations of the galaxy with parameters that reflect the inner parts of galaxies specifically at the galactic radius  $R=3\,\mathrm{kpc}$ . We find that differential rotation can induce a change in the parity of the magnetic field from an initially quadrupolar field to a dipolar field parity. These results are reproduced in fine detail by a modified version of the 1D model used in Qazi et al. (2023). Our simulations may explain why rotation measure synthesis of the galaxies NGC 4666 and NGC 4631 seem to suggest regular reversals in the sign of the Faraday depth along the major axis in the northern part of the galaxy. We attribute these regular reversals to the strength of differential rotation within the disc.

### 2 MODEL DESCRIPTION

The model and simulations used here are very similar to those of Qazi et al. (2023) but now include differential rotation. We model isothermal gas and magnetic field within a Cartesian box with x, y and z representing the radial, azimuthal and vertical directions, respectively. The simulation domain extends 4 kpc in each horizontal direction and 3 kpc vertically, centred at the galactic midplane. We have tested computational boxes of various sizes from 0.5 kpc to 16 kpc to confirm that we capture all essential features of the system. The grid resolution  $256 \times 256 \times 384$  mesh points, yielding the grid spacing about 15.6 pc along each dimension. The domain size is larger than the expected vertical and horizontal scales of the instability, and the resolution is sufficient to obtain convergent solutions to the instability model.

### 2.1 Basic equations

We consider a local rectangular box in a disc and introduce the rotating frame with a z-axis aligned with local angular velocity  $\Omega$ , the y-axis directed along the azimuth and the x-axis parallel to the local radial direction; the gravitational acceleration g is antiparallel to  $\Omega$ . We solve the non-ideal MHD equations for the gas density  $\rho$ , the velocity deviation from the overall rotation u and the magnetic vector potential A (which we solve for to ensure that the magnetic field is divergence-free). The system is initially in hydrostatic equilibrium

with a dynamically negligible seed magnetic field (of order  $10^{-3} \,\mu\text{G}$  in strength) required to launch the dynamo action. The shearing box approximation is used to implement differential rotation. The boundary conditions are periodic in x, sliding periodic in y and allow for the free exchange of matter through the top and bottom conditions (for further details, see Qazi et al. 2023). The governing equations

$$\frac{\mathrm{D}\rho}{\mathrm{D}t} = -\rho \nabla \cdot \boldsymbol{u} + \nabla \cdot (\zeta_D \nabla \rho) , \qquad (1)$$

$$\frac{\mathrm{D}\boldsymbol{u}}{\mathrm{D}t} = -g\hat{\boldsymbol{z}} - \frac{\nabla P}{\rho} + \frac{(\nabla \times \boldsymbol{B}) \times \boldsymbol{B}}{4\pi\rho} + \frac{\nabla \cdot (2\rho \nu \tau)}{\rho} - Su_x \hat{y} - 2\Omega \times \mathbf{u}$$

$$+ \nabla (\zeta_\nu \nabla \cdot \boldsymbol{u}) + \nabla \cdot (2\rho \nu_6 \tau^{(5)}) - \frac{1}{\rho} \boldsymbol{u} \nabla \cdot (\zeta_D \nabla \rho) , \qquad (2)$$

$$\frac{\partial \mathbf{A}}{\partial t} = \alpha \mathbf{B} + \mathbf{u} \times \mathbf{B} - Sa_{y}\hat{\mathbf{x}} - Sx \frac{\partial \mathbf{A}}{\partial y} - \eta \nabla \times \mathbf{B} + \eta_{6} \nabla^{(6)} \mathbf{A}, \qquad (3)$$

where  $D/Dt = \partial/\partial t + (U + u) \cdot \nabla$  is the advective derivative, P is thermal pressure, U = (0, Sx, 0) represents the global shear flow (differential rotation) in the local Cartesian coordinated with the shear rate  $S = r d\Omega / dr$  in terms of the cylindrical radius r) while **u** is the velocity deviation from the overall rotation  $U = Sx\hat{y}$ ; for a flat rotation curve,  $\Omega \propto r^{-1}$  and  $S = -\omega$ . We neglect the vertical gradients of the  $\Omega$  and S since the observed magnitude of the vertical gradient of U is of the order of  $20 \,\mathrm{km \, s^{-1} \, kpc^{-1}}$  (section 10.2.3 of Shukurov & Subramanian 2021, and referenced therein), leading to a relatively small velocity lag of order 30 km s<sup>-1</sup> at |z| = 1.5 kpc. We use the gravitational acceleration obtained for the Solar neighbourhood of the Milky Way by Kuijken & Gilmore (1989) and consider an isothermal gas with the sound speed  $c_s = 15 \,\mathrm{km \, s^{-1}}$ , which corresponds to a temperature of  $T = 2 \times 10^4$  K. Table 1 summarizes the parameter values adopted while Table 2 presents the simulations discussed in this paper. The traceless rate of strain tensor  $\tau$ has the form  $\tau_{ij} = \frac{1}{2}(\partial_j u_i + \partial_i u_j)$  (where  $\partial_i = \partial/\partial x_j$  and summation ober repeated indices is understood). The shock viscosity  $\zeta_{\nu} = v_{shock} f_{shock}$  in Equation 2, with  $f_{shock} \propto |\nabla \cdot \boldsymbol{u}_{-}|$  (where  $v_{shock}$  is a constant given in Table 1 and  $|\nabla \cdot u_-|$  is the divergence of the velocity field and it vanished otherwise) regularises shock fronts propagating perpendicular to steep pressure gradients, and differs from zero only in regions of converging flow (see Gent et al. (2020), for details). Following Gent et al. (2020), we also include the terms with  $\zeta_D$  in Equations 1 and 2 to ensure the momentum conservation. Similarly to  $\zeta_{\nu}$ , the shock capturing term in the continuity equation gas  $\zeta_D = D_{shock} f_{shock}$ , where  $D_{shock}$  is a constant given in Table 1. The hyperdiffusion with the coefficients  $nu_6$  and  $\eta_6$  is used to resolve grid-scale numerical instabilities, with  $\tau_{ij} = \frac{1}{2} \left[ \partial_i^5 u_j + \partial_i^4 (\partial_j u_i) \right] - \frac{1}{6} \partial_i^4 (\delta_{ij} \partial_k u_k) \text{ and } \nabla^{(6)} A_i = \partial_i^3 \partial_i^3 A_i,$ where  $\partial_i^n = \partial^n / \partial x_i^n$  (Brandenburg & Sarson 2002; Gent et al. 2021).

### 2.2 Boundary conditions

The boundary conditions in both horizontal directions x and y are periodic for all variables. To prevent an artificial inward advection of the magnetic energy through the top and boundary of the domain at  $z = \pm 1.5$  kpc, we impose the conditions  $B_x = B_y = 0$  and  $\frac{\partial B_z}{\partial z} = 0$ . The boundary conditions for the velocity field are stress-free

$$\frac{\partial u_z}{\partial z} = \frac{\partial u_y}{\partial z} = 0, \quad \text{at}|z| = 1.5$$
 (4)

To permit vertical gas flow across the boundaries without exciting numerical instabilities, the boundary condition for  $u_z$  imposes the

boundary outflow speed across the ghost zones outside the domain whereas an inflow speed at the boundary tends smoothly to zero across the ghost zones (Gent et al. 2013). The density gradient is kept at a constant level at the boundaries, with the scale height intermediate between that of the Lockman layer and the galactic halo.

$$\frac{\partial \ln \rho}{\partial z} = \pm \frac{1}{0.9 \,\text{kpc}} \quad \text{at} = \mp 1.5 \,\text{kpc}$$
 (5)

and we note that the value for the scale height has a negligible effect on the results.

### 2.3 The stratified gas layer

The gas is stratified by the application of vertical gravitational acceleration due to the stellar disc and dark matter halo following Kuijken & Gilmore (1989).

$$g = -a_1 \frac{z}{\sqrt{z_1^2 + z^2}} - a_2 \frac{z}{z_2},\tag{6}$$

with  $a_1 = 4.4 \times 10^{-14} \,\mathrm{km \, s^{-2}}$ ,  $a_2 = 1.7 \times 10^{-14} \,\mathrm{km \, s^{-2}}$ ,  $z_1 = 200 \,\mathrm{pc}$  and  $z_2 = 1 \,\mathrm{kpc}$ . We implement an altered version of this gravitational potential which accounts for the radial variation of the gravitational potential following Ferrière (1998).

$$g = -a_1 \frac{z}{\sqrt{z_1^2 + z^2}} \exp\left(-\frac{R - R_{\odot}}{a_3}\right) - a_2 \frac{R_{\odot}^2 + z_3^2}{R^2 + z_3^2} \frac{z}{z_2}$$

$$-2\Omega(\Omega + G)z.$$
(7)

with  $z_3 = 2.2$  kpc and  $a_3 = 4.9$  kpc. Using this gravitational potential and rotation curves taken from observations such as Clemens (1985) we hope to explore some of the impacts of the mean-dynamo in the inner galaxy. Although we aim to explore the interaction of the mean-field (turbulent) dynamo and the MBI and Parker instability, we do not simulate interstellar turbulence to keep the model better controllable and transparent. Instead, we impose the  $\alpha$ -effect with parameters typical of spiral galaxies, which drives the mean-field dynamo action. We use the same form of the  $\alpha$ -effect Qazi et al. (2023), antisymmetric in z, localized within a layer of thickness  $2h_{\alpha}$  around the midplane and smoothly vanishing at larger altitudes,

$$\alpha(z) = \alpha_0 \begin{cases} \sin(\pi z/h_\alpha), & |z| \le h_\alpha/2, \\ (z/|z|) \exp\left[-(2z/h_\alpha - z/|z|)^2\right], & |z| > h_\alpha/2. \end{cases}$$
(8)

The smaller  $h_{\alpha}$ , the stronger the vertical gradient of the magnetic field and the more it is buoyant. The seed magnetic field applied as an initial condition represents Gaussian random noise in the vector potential component  $A_z$  with a mean amplitude proportional to  $\rho^{1/2}(z)$  and the maximum strength  $10^{-6}$  mG at z=0. This field has  $B_z=0$ . A random initial magnetic field leads to shorter transients than in the case of a unidirectional initial field. In Sections 3-5 we explore generic features of the MBI and adopt  $h_{\alpha}=0.2$  kpc (equal to the initial density scale height) to make the instability stronger, to save computational resources and to allow for a more direct comparison with Qazi et al. (2023). The model parameters are adjusted to be closer the galactic conditions in Section 3 where we use values which reflect a radial distance in the galaxy of R=3 kpc.

 $h_{\alpha} = 0.3$  kpc and the solar neighbourhood value of the turbulent velocity  $\alpha_0 = 0.5$  km s<sup>-1</sup> (e.g. p.317 of Shukurov & Subramanian

**Table 1.** Parameters adopted in the numerical solutions of equations (1)–(3) in Sections ??–6.

Quantity	Symbol	Value	Unit
Grid resolution	$\delta x$	0.0156	kpc
Sound speed	$c_{\rm s}$	15	${\rm km}{\rm s}^{-1}$
Kinematic viscosity	ν	0.008, 0.3	$kpc km s^{-1}$
Magnetic diffusivity	$\eta$	0.03, 0.3	$kpc km s^{-1}$
$\alpha$ -effect magnitude	$\alpha_0$		${\rm km}{\rm s}^{-1}$
Dynamo scale height	$h_{\alpha}$	0.2,0.3	kpc
Magnetic diffusion time	$h_{m{lpha}}^2/\eta$	4/3,5/6	Gyr
Initial gas column density	$\Sigma$	$10^{21}$	$cm^{-2}$
Shock-capturing viscosity	$ u_{ m shock}$	1	kpc <sup>2</sup>
Shock-capturing diffusivity	$D_{ m shock}$	1	kpc <sup>2</sup>
Hyper-diffusivities	$\nu_6, \eta_6$	$10^{-12}$	$\rm kpc^5kms^{-1}$

2021). The dynamo intensity (in particular, the growth rate of the large-scale magnetic field) depends on the dimensionless parameters

$$R_{\alpha} = \alpha_0 h_{\alpha} / \eta$$
 and  $R_{\omega} = S h_{\alpha}^2 / \eta$ , (9)

which quantify the magnetic induction by the  $\alpha$ -effect and differential rotation, respectively. When  $R_{\alpha} \ll |R_{\omega}|$ , the magnetic field is mostly sensitive to their product known as the dynamo number,

$$D = R_{\alpha} R_{\omega} . \tag{10}$$

Qazi et al. (2023) considered a non-rotating system with an imposed  $\alpha$ -effect, a form of the mean-field dynamo known as the  $\alpha^2$ -dynamo. Here we include differential rotation to obtain a stronger magnetic field amplification mechanism known as the  $\alpha^2 \omega$ -dynamo.

# 3 EFFECTS OF THE CORIOLIS FORCE AND DIFFERENTIAL ROTATION

The system explored supports both  $\alpha\omega$  mean-field dynamo and the magnetic buoyancy instabilities, they are distinguished clearly during their linear stages when the corresponding perturbations grow exponentially, becoming strongly intertwined during the nonlinear stages of the instability when the Lorentz force becomes dynamically significant and the system evolves into a stationary state. During the nonlinear phase, it can become difficult to identify the role of each instability and Since the MBI is sensitive to the magnetic diffusivity and kinematic viscosity whereas the dynamo action is relatively insensitive to the kinematic viscosity; the first simulations use parameters similar to Qazi et al. (2023) adopting the parameter values used there, summarised in Table 1. The choice of a Prantdl number to be less than unity for the initial simulations will accentuate the effects of the MBI. We explored a range of different parameters which we presented in Table 2. The simulations in Tab 2 are chosen to represent two different possible rotation curves. Simulations R5 $\Omega$ 60S1-R5 $\Omega$ 60S01represent the situation with a flat rotation curve, whereas  $R5\Omega$ clemreflects a rotation curve of the Milky Way found in the observations of CO by Clemens (1985).

The growth rate for the most rapidly growing mode under the action of the mean-field dynamo, (Shukurov & Subramanian 2021, and references therein).

$$\gamma^{-1} = 1.5 \,\text{Gyr} (D_c - D)^{1/2} \left( \frac{h}{0.5 \,\text{kpc}} \right)^2 \left( \frac{l_0 v_0}{1 \,\text{kpc} \,\text{km} \,\text{s}^{-1}} \right)^{-1} \tag{11}$$

**Table 2.** Simulation runs with various values of dynamo numbers  $R_{\alpha}$  and  $R_{\omega}$ .  $\Omega$  is the angular velocity and  $\alpha_0$  is the corresponding  $\gamma_D$  is the rate of exponential growth of the magnetic field strength during the linear phase of the dynamo,  $\gamma_u$  is the growth rate of the root mean square gas speed.

Model	$R_{\alpha}$	$R_{\omega}$	$S \\ [\mathrm{km}\mathrm{s}^{-1}\mathrm{kpc}^{-1}]$		$\gamma_D$ [ km s <sup>-1</sup> ]	$\gamma_u$ [ kpc km s <sup>-1</sup> ]	Steady-state parity
R5Ω25S1	5	-33.4	-25	0.03	1.5	10.5	Dipolar
R10 $\Omega$ 25S1	10	-33.4	-25	0.03	8.4	3.8	Quadrupolar
R5 $\Omega$ clem	10	-33.4	-25	0.03	13.3	26.4	Quadrupolar
R5Ω60S1	5	-18	60	0.3	6.1	12.4	Quadrupolar
R5Ω60S07	5	-12.6	42	0.3	12.9	26.7	Dipolar
R5Ω60S05	5	-9	30	0.3	16.4	31.9	Dipolar
R5Ω60S03	5	-5.4	18	0.3	14.9	25.3	Dipolar
$R5\Omega60S01$	5	-1.8	9	0.3	13.7	28.2	Dipolar
R5Ω60S03CM	5	-1.8	9	0.3	15.9	18.0	Dipolar

for |D| > 100 Where  $D_c$  is the critical dynamo number along with  $l_0$  and  $v_0$  being the characteristic length and velocity. As shown in Fig 2, the growth rates obtained for the early stages of the magnetic field growth fit this dependence until we reach high dynamo numbers, which deviate from Eq 11. This may be understandable as the free decay modes which correspond to dipolar modes of the magnetic field decay much quicker than the quadrupolar modes, with the lowest quadrupolar modes decaying four times slower than the lowest nontrivial dipolar mode.

Figure 3 presents model R5 $\Omega$ 60S03, in which the growth rates and characteristic scale of the mean-field dynamo are different. The evolving spatial structure of the magnetic field is illustrated in Fig.1. At early times the field after the short-term transients from the initial condition have dissipated, the magnetic field is weak and has a relatively small scale imposed by the dynamo and is confined largely to the region  $|z| < h_{\alpha}$  where the  $\alpha$ -effect is imposed. At a later time, t = 1.1 Gyr the magnetic field spreads out from this region due to magnetic diffusion and we get the first signs of magnetic buoyancy, as seen by the enhancement of  $B_z$  (right-hand column of Fig.1). At that time, the growth rate of the magnetic field increases (Fig.3). In the strongly nonlinear stages ( $t > 1.1 \,\text{Gyr}$ ) the structure imposed by the dynamo has completely been removed despite the continued imposed  $\alpha$ -effect. Moreover, the field parity in the x and y components is now dipolar instead of the initially quadrupolar field generated by our imposed  $\alpha$ .

To illustrate three-dimensional field structures, including the prominent loops produced by the MBI and the magnetic field generated by the dynamo transformed by the MBI, Fig 4 shows the evolving three-dimensional structure of the magnetic field lines at various scales. The total magnetic field  $\mathbf{B}$  in this figure is separated into contributions  $B_B$  of the larger scales (characteristic of the MBI) and smaller ones  $B_D$  (driven by the imposed dynamo action) using Gaussian smoothing,

$$\boldsymbol{B}_{D}(x,t) = \int_{V} B(\boldsymbol{x}',t) G_{\ell}(\boldsymbol{x} - \boldsymbol{x}') d^{3}\boldsymbol{x}'$$
 (12)

where the integration extends over the whole domain volume with the smoothing kernel  $G_{\ell}(\zeta) = (2\pi\ell^2)^{-3/2} \exp\left[-|\zeta|^2/(2\ell^2)\right]$  with  $\ell = 200 \,\mathrm{pc}$ . Of note is that part of the small-scale field  $\boldsymbol{B}_D$  also contains random fields produced by nonlinear effects at the later stages of the system's evolution. The instability produces buoyant loops of a large-scale magnetic field at a kiloparsec scale. These 'Parker loops' are expected to lie largely in the azimuthal direction (The direction of the large-scale field) This corresponds to the 'undular' modes (with wavevector parallel to the magnetic field  $\mathbf{B}$ ) which are expected to dominate over the 'interchange' modes (with wavevector perpendicular to B) in linear analyses of the instability such as Matsumoto et al. (1993), such twisted loops are seen in Fig 5 which displays a small portion of the mean-field in the nonlinear stages of the system. These loops suggest possible observational signatures of the instability which may present in rotation measures or polarized synchrotron intensity maps, these observational signatures are explored by Rodrigues et al. (2015).

The restructuring of the magnetic field by the MBI is quantified in Fig 6, which shows the two-dimensional power spectra of the z-component of the magnetic field, of model R5 $\Omega$ 60S03, at times indicated above each frame. These confirm the evolution pattern visible in Fig 1. Over time the dominant horizontal scales  $2\pi k_x^{-1}$  and  $2\pi k_y^{-1}$  of the magnetic field grow larger: at  $t \leq 0.2$  the dominant  $k_v \approx 10 \, \mathrm{kpc}^{-1}$  is smaller whereas  $k_x$  is spans a larger array of values, this is in agreement with the analysis of Shu (1974) as the dominant azimuthal wavenumber  $k_y$  decreased under the influence of rotation. The dominant horizontal scales reduce to  $t = 1.3 \, \text{Gyr} \, k_x \approx 4 \, \text{and}$  $k_{\rm V} \approx 2$ , these wavenumbers correspond to scales over 1–2 kpc which are the characteristic scales of the MBI. As the peak wavenumbers decrease their spread is broader as the MBI excites a wider range of unstable modes.

### 4 NONLINEAR FIELD PARITY CHANGES

Figure 7 illustrates an even more fundamental consequence of the MBI under the effects of rotation: the magnetic field, which grows monotonically at early times develops a change in field parity at  $t \ge 1.1$  when it becomes strong enough to make the system essentially nonlinear. The figure shows the evolution of the horizontally averaged magnetic field components  $\langle B_x \rangle_{xy}$  and  $\langle B_y \rangle_{xy}$  from Model R5 $\Omega$ 60S03, normalized to their maximum values at each time to better expose the field structure at early times when it is still weak.

The linear evolution of all the models is similar with an exponential growth of the r.m.s magnetic field which results from the combined effects of our imposed  $\alpha$ -effect and the natural  $\Omega$ -effect from the differential rotation. Once the magnetic field is strong enough to become dynamically significant there is exponential growth of the r.m.s velocity. Once the kinetic and magnetic energies reach equipartition the magnetic field saturates and the system enters its nonlinear phase at which point the resultant field structures are vastly different. The magnetic field generated by the linear dynamo is confined to a relatively thin layer,  $|z| \lesssim h_{\alpha}$  and grows monotonically. However, it spreads to larger altitudes because of the buoyancy (to achieve the scale height of order 1 kpc). When fully nonlinear the magnetic field becomes undergoes a dramatic change in structure from an initially quadrupolar field structure to a now dipolar field structure in sim-

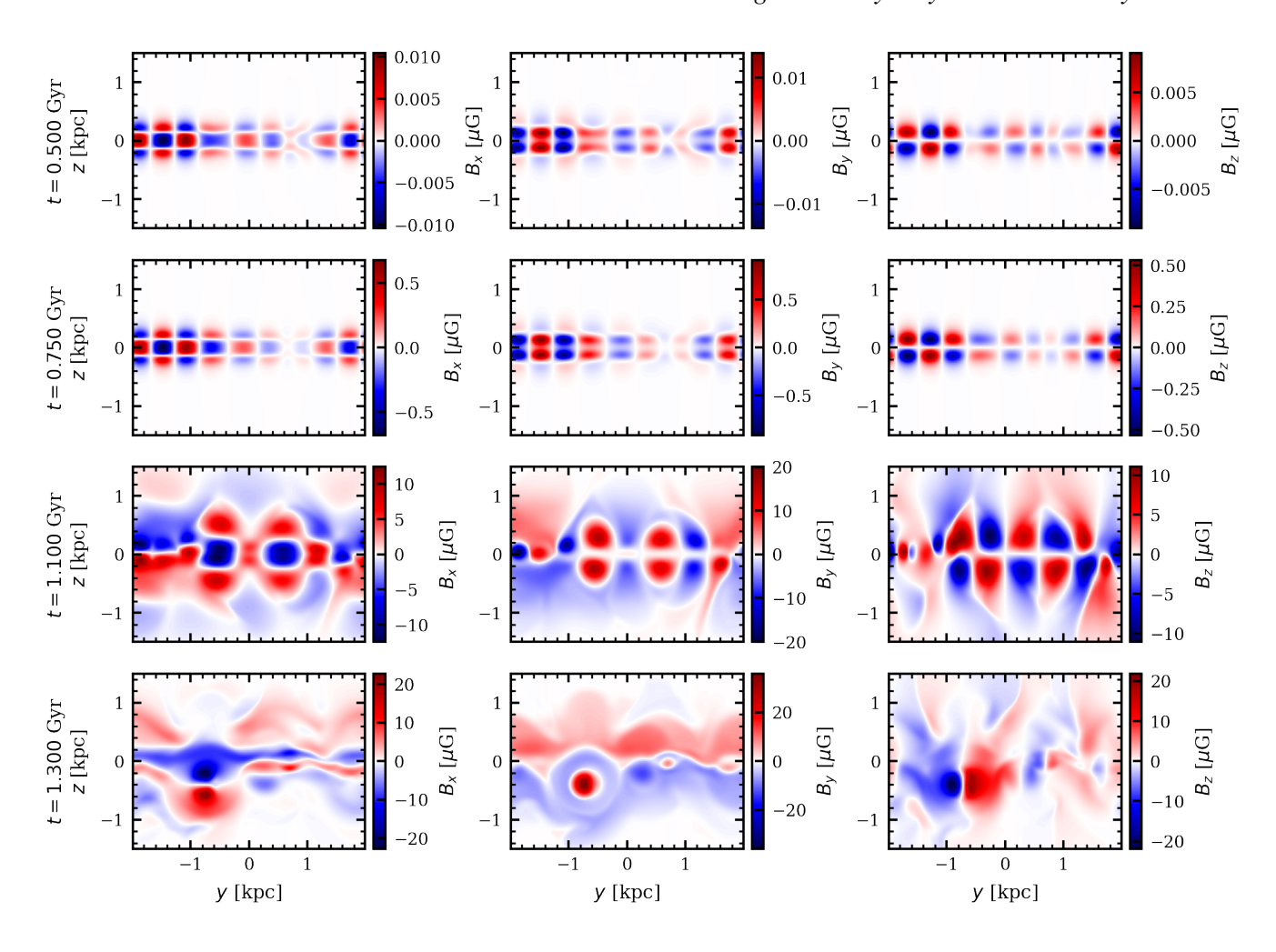
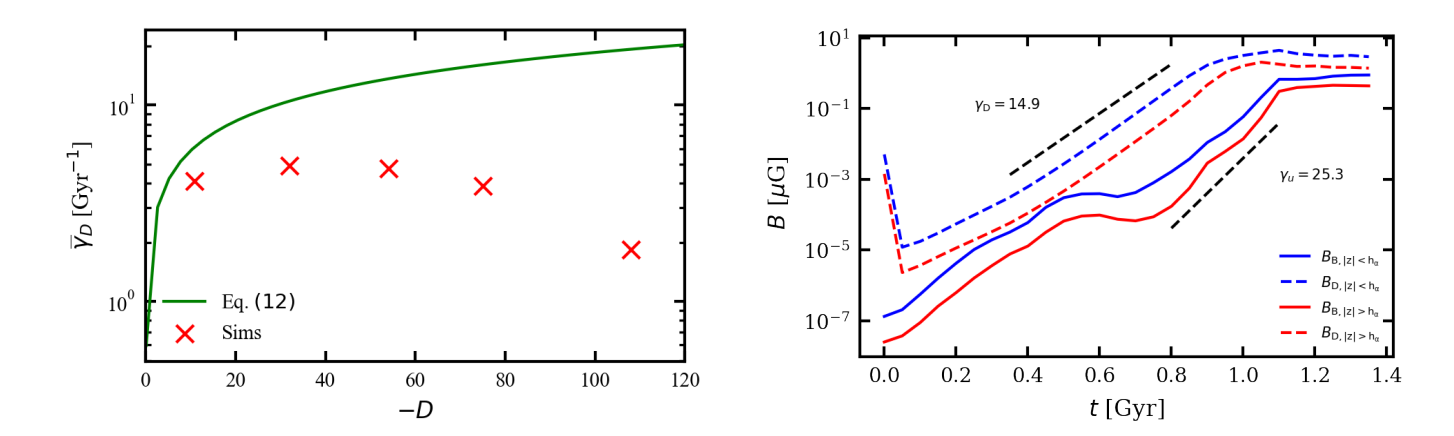


Figure 1. The strength of the horizontally averaged magnetic field components  $\langle B_X \rangle_{XY}$ ,  $\langle B_Y \rangle_{XY}$  and  $\langle B_Z \rangle_{XY}$  (columns from left to right) in the (y,z)-plane at various evolutionary stages: t = 0.5 Gyr and 0.75 Gyr (the two upper rows: the linear dynamo phase: the magnetic field strength grows while its spatial structure remains largely unchanged) and t = 1.1 Gyr and 1.3 Gyr (two bottom rows, early development of the MBI and the nonlinear stage) in Model R5Ω60S07. The nonlinear phase marks the appearance of large-scale vortical, in the magnetic field.



**Figure 2.** The dimensionless growth rates  $\bar{\gamma}_D = \gamma_D h_\alpha^2/\eta$  of the magnetic field at early times of the evolution when the dynamo action is predominant. The normalized expression of Eq 11

**Figure 3.** The evolving strengths of the large-(solid) and small scale (dashed) magnetic field (with scale separation of  $\ell=300\,\mathrm{pc}$ ) in model R5Ω60S03averaged over  $|z|< h_\alpha$  (blue) and  $|z|>h_\alpha$  (red). The dashed lines represent exponential growth rates in Gyr<sup>-1</sup> from Table 2.

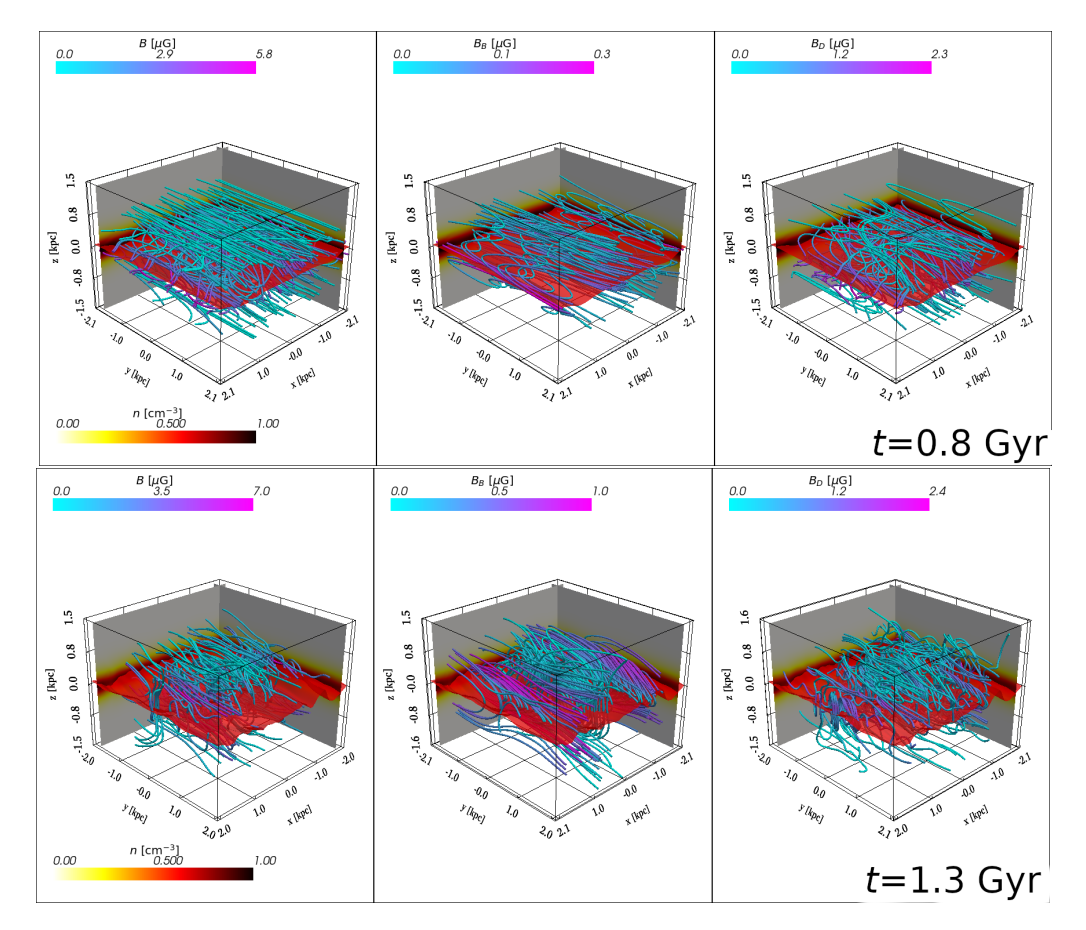


Figure 4. The magnetic lines in Model R5Ω60S03of the total field  $\mathbf{B}$  (left hand column), separated using a Gaussian kernel with a smoothing length  $\ell = 200$  pc into contributions at the larger scales characteristic of the magnetic buoyancy  $\mathbf{B}_B$  (middle) and the smaller scales of the imposed dynamo  $\mathbf{B}_D$  (right-hand column). The red isosurface corresponds to gas number density of 0.7 cm<sup>-3</sup>

ulations R5 $\Omega$ 60S07-R5 $\Omega$ 60S01. The resulting field structure in the nonlinear phase remains similar for all models that display the parity change.

## 4.1 Helical flows and dynamo driven by buoyancy modified by shear

The mean field induction equation can be written in terms of  $\langle \mathbf{B} \rangle$  as

$$\frac{\partial \langle \boldsymbol{B} \rangle}{\partial t} = \nabla \times (\langle \boldsymbol{u'} \rangle) \times \langle \boldsymbol{B} \rangle + \boldsymbol{\varepsilon} - \eta \nabla \times \langle \boldsymbol{B} \rangle \tag{13}$$

 $\varepsilon$  contributes the electromotive force (EMF) from averaging the turbulent fluctuations  $\langle u' \times B' \rangle$ . Applying a second-order correlation approximation to inhomogeneous, anisotropic turbulence as found in the ISM of a spiral galaxy, a general expression for the EMF has the form

$$\mathcal{E} = \alpha \cdot \langle \mathbf{B} \rangle + \gamma \times \langle \mathbf{B} \rangle - \beta \cdot (\nabla \times \langle \mathbf{B} \rangle)$$
$$-\delta \times (\nabla \times \langle \mathbf{B} \rangle) - \kappa \cdot (\nabla \langle \mathbf{B} \rangle)^{(s)}$$
(14)

in which tensors  $\alpha$  and  $\beta$  are second order and  $\kappa$  is third order. Each of these terms represents a physical process. The  $\alpha$  tensor applies effects from small-scale helicity,  $\beta$  turbulent diffusivity,  $\delta$  turbulent pumping,  $\gamma$  shear or rotating current effects, and  $\kappa$  includes the residual effects, depending on the symmetric part of the magnetic gradient tensor  $(\nabla \langle B \rangle)^{(s)}$ . A comprehensive study of each of these

effects will be required to explain fully the mean-field dynamo, but we focus on  $\alpha$ . Some indication of EMF properties may be extracted from our imposed  $\alpha$ -effect term. The action of the Coriolis force on the sheared, vertically stratified disc will tend to inject helicity into the systemic vertical flows of opposite signs on either side of the midplane. The dynamo amplifies a magnetic field with opposing small-scale helicity, which will quench the dynamo if it can not be removed (Brandenburg & Subramanian 2005; Shukurov & Subramanian 2021). Under the assumption of homogeneous isotropic turbulence  $\alpha$  can be reduced to a scalar

$$\alpha = \alpha_k + \alpha_m \tag{15}$$

The kinetic helicity contributes to the mean-field dynamo as

$$\alpha_k \approx -\frac{1}{3}\tau \langle \boldsymbol{u}' \cdot \boldsymbol{\omega}' \rangle \tag{16}$$

where  $\tau$  is the correlation time of the turbulence and  $\Omega' = \nabla \times u'$  is its vorticity (Moffatt 1978; Krause & Rädler 1980). Due to the conservation of magnetic helicity, for the mean-field dynamo to exist some small-scale helicity flux is required (Pouquet et al. 1976; Brandenburg & Subramanian 2005). The magnetic helicity contributes to the mean-field dynamo as

$$\alpha_{m} \approx \frac{1}{3} \tau \left\langle \frac{(\nabla \times \mathbf{B})' \cdot \mathbf{B'}}{\rho} \right\rangle \tag{17}$$

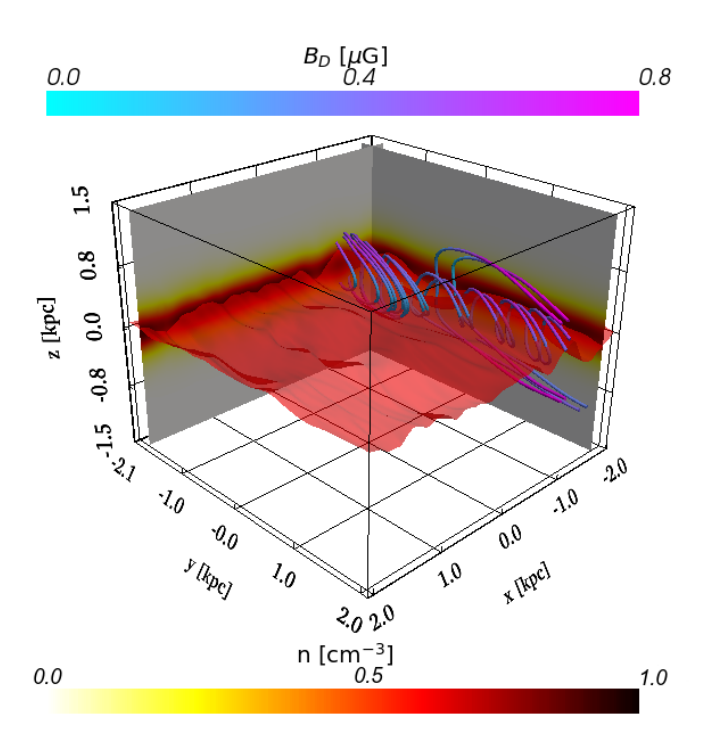


Figure 5. Portion of the mean-field  ${\pmb B}_B$  taken from Fig 4, where the Parker loops are easily identifiable

These simplified expressions can be used to see how the Lorentz force acts against the flow as the dynamo approaches saturation, where the opposite sign of  $\alpha_M$  can lead to  $\alpha$ -quenching. We approximate the proxy for  $\alpha = \alpha_K + \alpha_M$  in equations (15) and (16). Since our simulations in Tab 2 include rotation, the mean helicity of the flow  $\langle \boldsymbol{u} \cdot (\nabla \times \boldsymbol{u}) \rangle$  can be driven by both the Lorentz and Coriolis forces. The Coriolis force in a stratified, rotating system is the cause of the conventional  $\alpha$ -effect with  $\alpha_k > 0$  for z > 0 and  $\alpha_k(-z) = -\alpha_k(z)$  (Shukurov & Subramanian 2021, e.g., Section 7.1 of).

As with Qazi et al. (2023) at t > 0.75 Gyr, at the onset of the nonlinearity, magnetic spreads the magnetic field out of the layer  $|z| < h_{\alpha}$  which buoyancy, which is reflected in the region  $0.75\,\mathrm{Gyr} \le t \le 1.0\,\mathrm{Gyr}$ . While there asymmetry of  $\alpha_k$  in z is evident in Fig 8, the sign of  $\alpha_k$  is opposite to that of the  $\alpha$  produced by the Coriolis force which is clearly shown for  $t > 1.2 \,\mathrm{Gyr}$ . The imposed mean-field dynamo action near the midplane, with  $\alpha$  as given in Equation 8 has the conventional sign, with  $\alpha > 0$  at z > 0. The opposite sign of the kinetic helicity implies that helical motion produced by imposed dynamo saturates the dynamo action imposed dynamo action in the layer near the midplane (Shukurov & Subramanian 2021, e.g., Section 7.11 of). After some time there is the generation of helicity with the conventional sign which is generated at altitudes of  $|z| > h_{\alpha}$ , this additional dynamo action, which we attribute to the Coriolis force is responsible for the dramatic change in field parity. As expected the sign of  $\alpha_m$  is shown in the lower panel of Figure 8 which as expected has the opposite sign to that of  $\alpha_k$  and a comparable magnitude.

### 5 ELECTROMOTIVE FORCE AND TRANSPORT COEFFICIENTS

To verify further and justify our interpretation of the results, we have computed the components of the (pseudo-)tensor  $\alpha_{ij}$  and tensor  $\beta_{ij}$  using the method of iterative removal of sources (IROS) introduced by Bendre et al. (2023). Using the time series for the components of the electromotive force  $\mathcal{E}_i = \langle u \times b \rangle_i$  are approximated by  $\mathcal{E}_i = \alpha_{ij} \langle \mathbf{B}_i \rangle - \beta_{ij} (\nabla \times \langle \mathbf{B} \rangle)_i$ . Explicitly,

$$\begin{pmatrix} \mathcal{E}_{x} \\ \mathcal{E}_{y} \end{pmatrix} = \begin{pmatrix} \alpha_{xx} & \alpha_{xy} \\ \alpha_{yx} & \alpha_{yy} \end{pmatrix} \begin{pmatrix} \langle B \rangle_{x} \\ \langle B \rangle_{y} \end{pmatrix} - \begin{pmatrix} \beta_{xx} & \beta_{xy} \\ \beta_{yx} & \beta_{yy} \end{pmatrix} \begin{pmatrix} (\nabla \times \langle \mathbf{B} \rangle)_{x} \\ (\nabla \times \langle \mathbf{B} \rangle)_{y} \end{pmatrix}$$
(18)

are solved to determine the elements of the tensors  $\alpha_{ij}$  and  $\beta_{ij}$ , which are assumed to be independent of time. This assumption is valid in either the early stages of the exponential growth of the magnetic field or in the later, stationary state of the system. In these calculations horizontal averaging is used,  $\langle {\bf B} \rangle = \langle {\bf B} \rangle_{xy}$ , as displayed in Fig. 7, such that the tensor elements are functions of z alone. The horizontal average of the vertical component of the magnetic field vanishes due to the horizontal periodic boundary conditions. Hence, the analysis is applied only to the horizontal components of the magnetic field.

When the mean gas velocity vanishes (as it does in this case) the equation for the mean magnetic field has the form

$$\frac{\partial \langle \mathbf{B} \rangle}{\partial t} = \nabla \times (\mathcal{E} - \eta \nabla \times \langle \mathbf{B} \rangle) \tag{19}$$

the diagonal elements of the  $\alpha$ -tensor represent the  $\alpha$ -effect with  $\alpha_k + \alpha_m \approx \frac{1}{2}(\alpha_{xx} + \alpha_{yy})$ . If the flow is isotropic in the (x,y)-plane  $\alpha_{i,j}$  is antisymmetric  $(\alpha_{yx} = -\alpha_{xy})$  and the off-diagonal elements represent the transfer of the mean magnetic field along the z-axis at the effective speed  $U_z = -\alpha_{xy}$  due to the increase in the turbulent magnetic diffusivity with |z| resulting mainly from the increase of the random flow speed (turbulent diamagnetism – e.g., Section 7.9 of Shukurov & Subramanian 2021). The diagonal components of the tensor  $\beta_{ij}$  represent the turbulent magnetic diffusion.

Figure 9 presents the resulting components of the tensors  $\alpha_{ij}$  and  $\beta_{ij}$  for the non-linear stage of the evolution. The yellow stripes represent one standard deviation of the variables obtained from five estimates, each resulting from the sampling of every fifth entry in the times series of  $\mathcal{E}$  containing 1500 data points at each z, measured with the time interval 1 Myr.

 $\alpha_{xx} + \alpha_{yy}$  is significant in magnitude, antisymmetric with respect to the midplane z=0 and mostly negative at z>0. The magnitudes of  $\alpha_{xx}$  and  $\alpha_{yy}$  are close to  $\alpha_k + \alpha_m$  obtained using equations (16) and (17) with the time interval 1 Myr. The off-diagonal components of the  $\alpha_{ij}$  are quite close to the expected antisymmetry,  $\alpha_{yx} = -\alpha_{xy}$  and reflect the transfer of the mean magnetic field toward the midplane z=0 which is associated with the increase of the turbulent magnetic diffusivity with |z|, which will oppose the buoyancy migration of the magnetic field away from the midplane.

 $\alpha_{ij}$  and  $\beta_{ij}$  fluctuate around the zero level during the linear stage of the evolution without any significant effect on the evolution.

### 6 ONE-DIMENSIONAL MODEL OF SWITCH IN PARITIES

In this section, we propose a nonlinear one-dimensional model of the mean-field dynamo with advection due to magnetic buoyancy and demonstrate that it not only admits parity switches seen in the models presented but also reproduces quantitatively the resultant

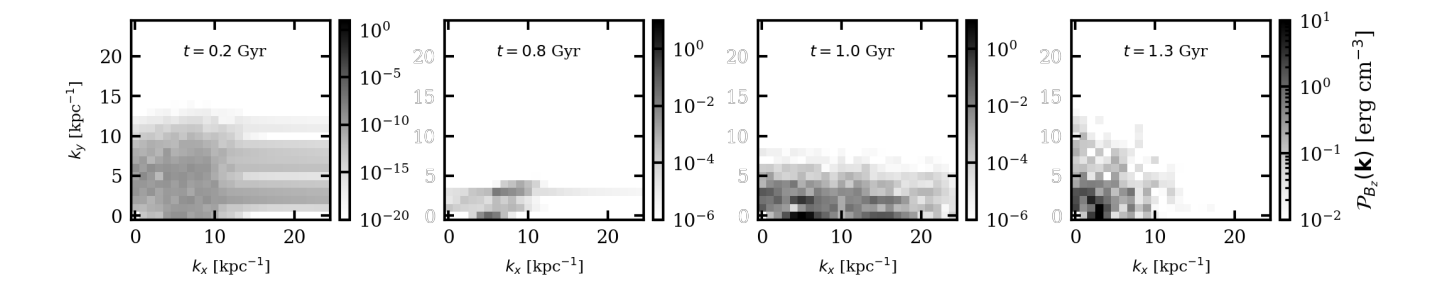
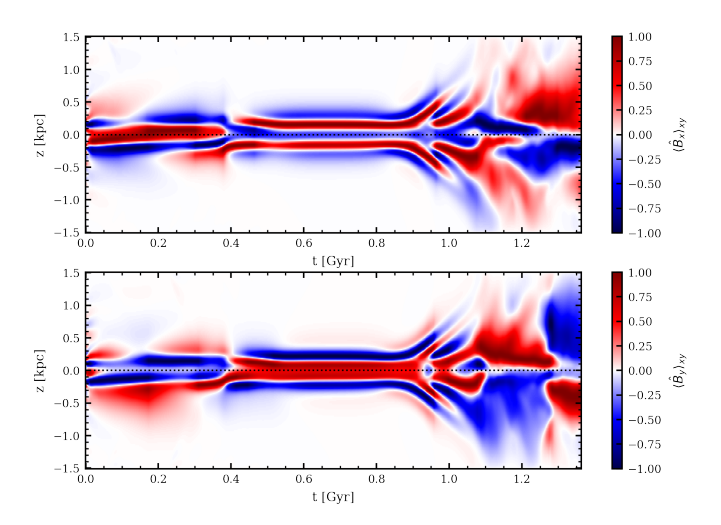
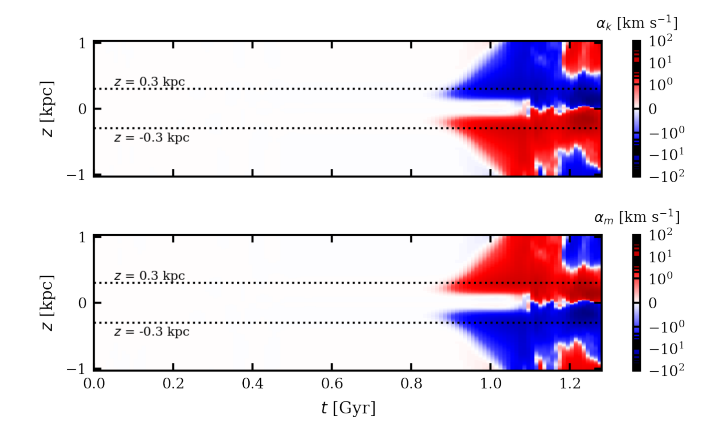


Figure 6. Two-dimensional power spectra in the  $(k_x, k_y)$ -plane of  $B_z$  in Model R5 $\Omega$ 60S03at z = 385 pc during the dominance of the mean-field dynamo (leftmost and middle panels) and a stationary state (right).



**Figure 7.** The evolution of the horizontally averaged magnetic field components  $\langle \widehat{B_X} \rangle_{xy}$  (upper panel) and  $\langle \widehat{B_y} \rangle_{xy}$  (lower panel) in Model R5 $\Omega$ 60S03normalized to their maximum values at each time.



**Figure 8.** The evolution of the horizontally averaged mean kinetic helicity (upper panel) and mean magnetic helicity (lower panel) coefficients of the random velocity and magnetic fields, Equations 16 and ?? respectively, in Model R5Ω60S03, The horizontal dotted lines are shown at  $|z| = h_{CC}$ .

field as discussed above. Improving upon the model shown in Qazi et al. (2023) we include the effects of differential rotation and now account for the complex structure of the kinetic helicity generated in the nonlinear phase by magnetic buoyancy and differential rotation. The x- and y- components of the mean-field dynamo equation

$$\frac{\partial B_x}{\partial t} = -\frac{\partial}{\partial z}(\alpha B_y) + \beta_z \frac{\partial^2 B_x}{\partial z^2} - \frac{\partial}{\partial z}(B_x U_z - U_x B_z) \tag{20}$$

$$\frac{\partial B_y}{\partial t} = -\frac{\partial}{\partial z}(\alpha B_x) + \beta_z \frac{\partial^2 B_y}{\partial z^2} - \frac{\partial}{\partial z}(B_y U_z - U_y B_z) + S_0 B_x \quad (21)$$

$$\frac{\partial B_z}{\partial t} = \alpha(B_y) + \beta \frac{\partial^2 B_z}{\partial z^2} - \frac{\partial}{\partial z} (B_z U_z)$$
 (22)

where  $U_x = U_y = 1 \, \mathrm{km \, s^{-1}}$  and  $S_0 = -25 \, \mathrm{km \, s^{-1}} \, \mathrm{kpc^{-1}}$  is the shear rate and we assume that all variables only depend on t and z (the infinite slab approximation), we also omit the brackets denoting the averaging to simplify notation in this section. The averaging condition used here crucially could not be a horizontal average since the field average in the horizontal (x,y)-plane is a function of z alone. Combined with  $\nabla \cdot \mathbf{B} = 0 \rightarrow \partial \langle B_z \rangle / \partial z$  and although this type of horizontal averaging satisfies the Reynolds rules of averaging these types of restrictions limit the admissible structure of the magnetic field, without any physical or mathematical justification, if such an averaging method were used then there could be no evolution equation for  $B_z$ .

This indicates that important information is lost when considering a horizontally averaged field and that the horizontal spatial structure of all components of the magnetic field should be accounted for as they may produce non-trivial effects. The advection velocity  $U_z$  satisfies the Navier-Stokes equation

$$\frac{\partial U_z}{\partial t} - U_z \frac{\partial U_z}{\partial z} = v \frac{\partial^2 U_z}{\partial z^2} - \frac{1}{8\pi\rho} \frac{\partial B^2}{\partial z} + \frac{\rho'}{\rho_0} g \tag{23}$$

where g is the vertical acceleration due to gravity and the second term on the right-hand side is the Archimedes force resulting from magnetic buoyancy. We neglect the time variation of the gas density, adopting  $\rho=\rho_0$  at all times but, in the spirit of the Boussinesq approximation, include density variation  $\rho'$  in the Archimedes force. Consider a region of density  $\rho=\rho_0+\rho'$  containing a magnetic field of a strength B+b surrounded by the gas of the density  $\rho_0$  with magnetic field B (here B is the mean field strength and b is its local perturbation). The pressure balance in an isothermal gas then leads to

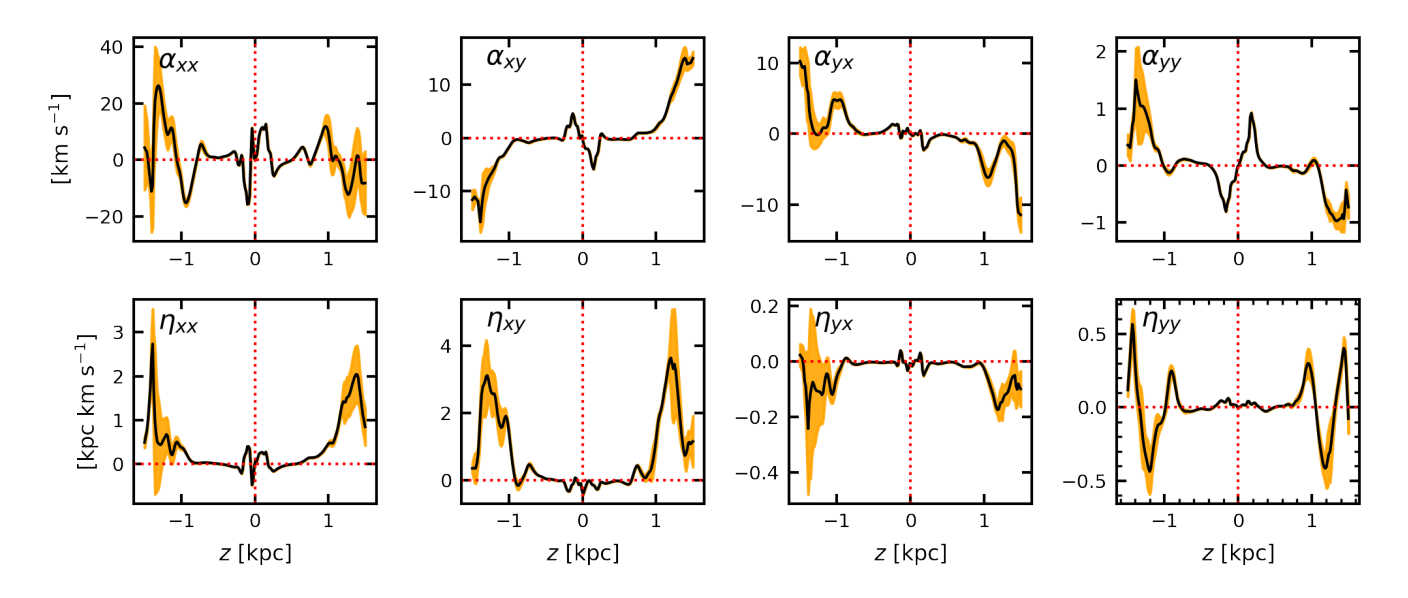


Figure 9. The elements of the turbulent transport tensor introduced in Equation 18 for model R5 $\Omega$ 60S03in the nonlinear state at 1.0 < t < 1.5 Gyr. The yellow stripes indicate one standard deviation of the variables based on bootstrap resampling of the time series of  $\mathcal{E}$ .

$$\rho' = -\frac{2Bb + b^2}{8\pi c_s^2} \tag{24}$$

To replicate the complex structure of the kinetic  $\alpha$ -effect in the nonlinear stages of the dynamo as seen in Figure 8, we choose the following for of  $\alpha(z,t)$ ,

$$\alpha(z,t) = \begin{cases} \alpha_0 \sin(\pi z/h_\alpha), & |z| \le h_\alpha/2\\ \alpha_1(z,t) \frac{z}{|z|} \exp\left[-\left(\frac{2z}{h_\alpha} - \frac{z}{|z|}\right)^2\right], & |z| > h_\alpha/2 \end{cases}$$
(25)

$$\alpha_1(z,t) = \alpha_0 \frac{t_f - t}{t_f} + \alpha_0 \tanh\left(\frac{\pi z}{h_\alpha} - \frac{z\pi}{|z|}\right)$$
 (26)

where  $t_f$  is the time at which the magnetic field saturates in the 3D model. The  $\alpha$ -effect used here is not subject to the same  $\alpha$ -quenching implemented in Qazi et al. (2023) however when included the picture is unchanged. Equations (20)-(23) are solved numerically in  $0 < z < z_0$  with  $z_0 = 1.5$  kpc.  $U_z, B_x, B_y$  and  $B_z$  are symmetric about z = 0 (a quadrupolar magnetic structure and known to dominate within a thin layer - e.g., Section 11.3.1 of Shukurov & Subramanian 2021) with

$$\frac{\partial B_x}{\partial z} = \frac{\partial B_y}{\partial z} = \frac{\partial B_z}{\partial z} = U_z = 0 \tag{27}$$

At  $z=z_0$  we apply an impenetrable boundary condition for  $U_z$ , and vacuum boundary conditions for the magnetic field

$$U_z = B_x = B_y = B_z = 0 (28)$$

We justify this by the fact that the turbulent magnetic diffusivity increases with |z| (see Section 11.3 of Shukurov & Subramanian 2021, for details). Larger vertical sizes were used to confirm the domain was large enough to prevent any spurious boundary effects

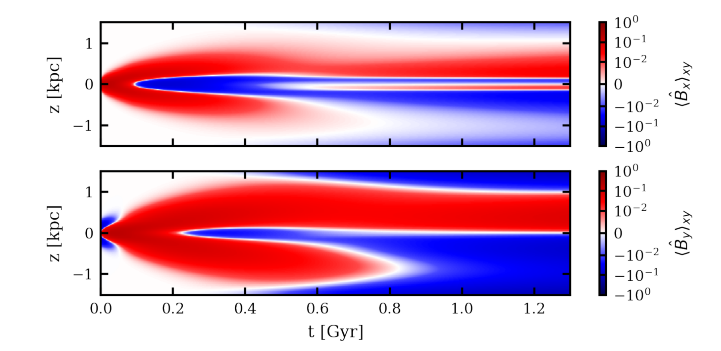


Figure 10. The evolution of the horizontally averaged magnetic field components  $\langle \widehat{B}_x \rangle_{xy}$  (upper panel) and  $\langle \widehat{B}_y \rangle_{xy}$  (lower panel) in model R5Ω60S03 normalized to their maximum values at each time.

over the simulation period. The initial magnetic field has a strength of 1 mG.

Figure 10 shows the evolution of the horizontally averaged components of the magnetic field and also shows the switch in field parties. We do not attempt to achieve a precise match between the three-dimensional and one-dimensional results being content with the fact that the one-dimensional model justifies further our conclusion that the change in field parity are nonlinear phenomena that rely on the interaction of the mean-field dynamo and the rotational shear.

### 7 COSMIC RAYS AND THE GALACTIC DYNAMO

We model cosmic rays in a way similar to Tharakkal et al. (2023a) and Rodrigues et al. (2015) using a fluid approximation (e.g. Parker & Lerche (1969); Schlickeiser & Lerche (1985)) where the cosmic ray energy density  $\epsilon_{CR}$  is governed by

$$\frac{\partial \epsilon_{CT}}{\partial t} + \nabla \cdot (\epsilon_{CT} \boldsymbol{u}) + p_{CT} \nabla \cdot \boldsymbol{u} + Q(z) = -\nabla \cdot \boldsymbol{F}$$
 (29)

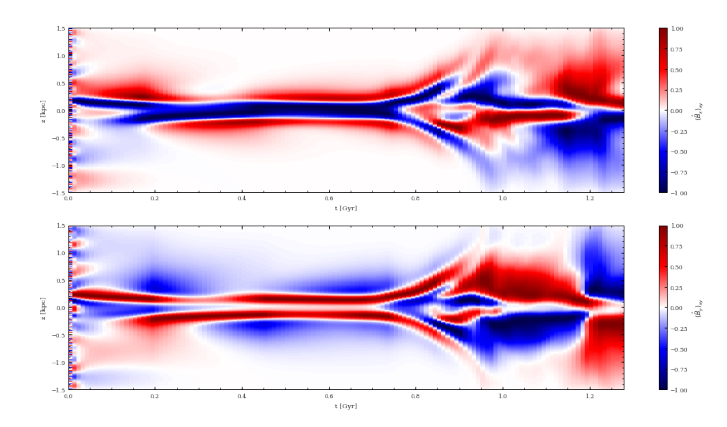


Figure 11. Horizontal averages of the horizontal components of the magnetic field  $\langle B_X \rangle_{XY}$ ,  $\langle B_Y \rangle_{XY}$  in Model R5Ω60S03CM.

with F the cosmic ray flux defined below and Q(z) a source term with the form

$$Q(z) = \epsilon_{cr,0} exp\left(-\left(\frac{|z|}{h_{cr}}\right)^2\right)$$
(30)

The source term is chosen to replicate the injection of cosmic rays into the ISM by supernovae. The typical supernovae explosion (SNe) ejects a mass with  $M_{ej}$  with a kinetic energy  $E_0 = 10^{51}$  erg, roughly 10% of the energy is converted into cosmic ray energy, these SNe are expected to occur within a roughly 100 pc disc. To replicate this situation we choose the scale height of the energy injection to be  $h_{cr} = 100$  pc and  $\epsilon_{cr,0} = 10^{50}$ .

Figure 11 presents the horizontal averages for the Model R5 $\Omega$ 60S03CM, including cosmic rays. Cosmic rays exert considerable pressure and have negligible weight, enhancing the effects of magnetic buoyancy and subsequently making the dynamo and instability stronger. The trend of Table 2 suggests that stronger buoyancy would cause the field parity in the nonlinear stages of the system to be quadrupolar. However, despite the enhancement to the buoyancy the parity in the nonlinear stages of the system is still dipolar.

### **8 CONCLUSIONS**

The rotation speed reduces with distance from the disc of the spiral galaxy, this has been firmly established by observation of neutral and ionized hydrogen. Levine et al. (2008) find  $\partial V_\phi \partial/|z| = -(22\pm 6)~{\rm km\,s^{-1}}$  within  $|z|=100~{\rm pc}$  of the Galactic midplane near the sun. Since the  $D\sim\Omega^2$  this will dramatically weaken the mean-field dynamo at larger altitudes and because this switch in dipolar parity requires dynamo action at larger altitudes. If vertical variation of the rotation speed were accounted for the switch to dipolar parity would require a stronger mean-field dynamo.

### ACKNOWLEDGEMENTS

The raw data for this work were obtained from numerical simulations using the open-source PENCIL-CODE available at https://github.com/pencil-code. The derived data used for analysis are available on request from Yasin Qazi.

### DATA AVAILABILITY

The inclusion of a Data Availability Statement is a requirement for articles published in MNRAS. Data Availability Statements provide a standardised format for readers to understand the availability of data underlying the research results described in the article. The statement may refer to original data generated in the course of the study or to third-party data analysed in the article. The statement should describe and provide means of access, where possible, by linking to the data or providing the required accession numbers for the relevant databases or DOIs.

#### REFERENCES

Bendre A. B., Schober J., Dhang P., Subramanian K., 2023, Iterative removal of sources to model the turbulent electromotive force (arXiv:2308.00059)

Brandenburg A., Sarson G. R., 2002, Phys. Rev. Lett., 88, 055003

Brandenburg A., Subramanian K., 2005, Phys. Rep., 417, 1

Clemens D. P., 1985, ApJ, 295, 422

Ferrière K., 1998, ApJ, 497, 759

Foglizzo T., Tagger M., 1994, A&A, 287, 297

Foglizzo T., Tagger M., 1995, A&A, 301, 293

Gaburov E., Johansen A., Levin Y., 2012, ApJ, 758, 103

Gent F. A., Shukurov A., Sarson G. R., Fletcher A., Mantere M. J., 2013, MNRAS, 430, L40

Gent F. A., Mac Low M. M., Käpylä M. J., Sarson G. R., Hollins J. F., 2020, Geophysical and Astrophysical Fluid Dynamics, 114, 77

Gent F. A., Mac Low M.-M., Käpylä M. J., Singh N. K., 2021, ApJ, 910, L15 Giz A. T., Shu F. H., 1993, ApJ, 404, 185

Hanasz M., Lesch H., 1997, A&A, 321, 1007

Johansen A., Levin Y., 2008, A&A, 490, 501

Kim J., Hong S. S., Ryu D., 1997, ApJ, 485, 228

Krause F., R\u00e4dler K.-H., 1980, Mean-Field Magnetohydrodynamics and Dynamo Theory. Pergamon Press (also Akademie-Verlag: Berlin), Oxford Kuijken K., Gilmore G., 1989, MNRAS, 239, 571

Levine E. S., Heiles C., Blitz L., 2008, The Astrophysical Journal, 679, 1288
Machida M., Nakamura K. E., Kudoh T., Akahori T., Sofue Y., Matsumoto R., 2013, ApJ, 764, 81

Matsumoto R., Tajima T., Shibata K., Kaisig M., 1993, ApJ, 414, 357

Moffatt K., 1978, The Generation of Magnetic Fields in Electrically Conducting Fluids. Cambridge University Press, Cambridge

Moss D., Shukurov A., Sokoloff D., 1999, A&A, 343, 120

Newcomb W. A., 1961, Phys. Fluids, 4, 391

Parker E. N., 1979, Cosmical Magnetic Fields: Their Origin and Their Activity. Clarendon Press, Oxford

Parker E. N., Lerche I., 1969, Comments on Astrophysics and Space Physics, 1, 215

Pouquet A., Frisch U., Léorat J., 1976, Journal of Fluid Mechanics, 77, 321–354

Qazi Y., Shukurov A., Tharakkal D., Gent F. A., Bendre A. B., 2023, arXiv e-prints, p. arXiv:2310.08354

Rodrigues L. F. S., Shukurov A., Fletcher A., Baugh C. M., 2015, MNRAS, 450, 3472

Rodrigues L. F. S., Sarson G. R., Shukurov A., Bushby P. J., Fletcher A., 2016, ApJ, 816, 2

Schlickeiser R., Lerche I., 1985, A&A, 151, 151

Shu F. H., 1974, A&A, 33, 55

Shukurov A., Subramanian K., 2021, Astrophysical Magnetic Fields: From Galaxies to the Early Universe. Cambridge University Press, Cambridge, doi:10.1017/9781139046657

Tharakkal D., Shukurov A., Gent F. A., Sarson G. R., Snodin A., 2023a, MNRAS, 525, 2972

Tharakkal D., Shukurov A., Gent F. A., Sarson G. R., Snodin A. P., Rodrigues L. F. S., 2023b, MNRAS, 525, 5597

### APPENDIX A: SOME EXTRA MATERIAL

If you want to present additional material which would interrupt the flow of the main paper, it can be placed in an Appendix which appears after the list of references.

This paper has been typeset from a TEX/LATEX file prepared by the author.